# Structural and functional MRI reveals multiple retinal layers

Haiying Cheng[†], Govind Nair[†], Tiffany A. Walker[‡], Moon K. Kim[‡], Machelle T. Pardue[‡§], Peter M. Thulé[¶‖], Darin E. Olson[¶‖], and Timothy Q. Duong[†,††]

[†]Yerkes Imaging Center and Department of Neurology and Radiology, [§]Department of Ophthalmology, and [¶]Division of Endocrinology, Metabolism, and Lipids, Emory University, Atlanta, GA 30329; and [‡]Rehabilitation Research and Development Center and [‖]Research Service, Department of Veterans Affairs Medical Center, Atlanta, GA 30033

Edited by Marcus E. Raichle, Washington University School of Medicine, St. Louis, MO, and approved September 20, 2006 (received for review July 10, 2006)

**MRI is a noninvasive diagnostic modality that reveals anatomy, physiology, and function *in vivo* without depth limitation or optical interference. MRI application to the retina, however, remains challenging. We improved spatial resolution to resolve layer-specific structure and functional responses in the retina and confirmed the laminar resolution in an established animal model of retinal degeneration. Structural MRI of normal rat retinas revealed three bands corresponding histologically to (*i*) the combined ganglion cell layer/inner nuclear layer plus the embedded retinal vessels, (*ii*) the avascular outer nuclear (photoreceptor) layer and its photoreceptor segments, and (*iii*) the choroidal vascular layer. Imaging with an intravascular contrast agent (gadolinium-diethylene-tri-amine-pentaacetic acid) enhanced the retinal and choroidal vascular layers bounding the retina, but not the avascular outer nuclear layer and the vitreous. Similarly, blood-oxygen-level-dependent (BOLD) functional MRI revealed layer-specific responses to hyperoxia and hypercapnia. Importantly, layer-specific BOLD responses in the two vascular layers were divergent, suggesting the two vasculatures are differentially regulated. To corroborate sensitivity and specificity, we applied layer-specific MRI to document photoreceptor degeneration in Royal College of Surgeons rats. Consistent with histology, layer-specific MRI detected degeneration of the outer nuclear layer. Surprisingly, MRI revealed increased thickness in the choroidal vascular layer and diminished BOLD responses to hyperoxia and hypercapnia in the Royal College of Surgeons rat retinas, suggesting perturbation of vascular reactivity secondary to photoreceptor loss. We conclude that MRI is a powerful investigative tool capable of resolving lamina-specific structures and functional responses in the retina as well as probing lamina-specific changes in retinal diseases.**

columnar resolution | high-resolution functional MRI | lamina-specific MRI | retinal degeneration

The diagnosis of retinal disease relies on the demonstration of structural or functional alterations in the retina or its vasculature. Fundus photography and optical coherence tomography (1) have made critical contributions to the diagnosis of disease-induced structural changes, whereas blood-flow abnormality in the retina can be measured by using fluorescein angiography, indocyanin-green angiography, and laser Doppler flowmetry (2). Functional imaging of the retina was recently reported using intrinsic optical imaging (3). However, laminar resolution of deep retinal layers using these modalities is confounded by strong tissue absorption, optical scattering, and disease-induced opacity of the vitreous humor, cornea, and lens (such as vitreal hemorrhage and cataract). Although recent advances in optical coherence tomography allow structural layer resolution, optical techniques are generally limited to probing the proximal retina and large surface vessels.

In contrast, MRI has no depth limitation and is widely used to noninvasively study anatomy, physiology, and function in a single setting. Structural MRI provides detailed anatomical images *in vivo*. Concomitant use of an i.v. contrast agent [such as gadolinium-diethylene-tri-amine-pentaacetic acid (Gd-DTPA)] selectively enhances vascular structures and reveals disease-induced vascular permeability changes. The development of functional MRI (fMRI), such as blood-oxygen-level-dependent (BOLD) fMRI, has revolutionized brain mapping by providing noninvasive, real-time visualization of brain function (4). Although the spatial resolution of MRI is lower than optical and histologic techniques, recent advances have made fMRI of cortical columns (5–7) and laminar structures (8, 9) possible. However, even higher spatial resolution and contrast are required if MRI is to be successfully applied to the retina.

The retina can be organized into three major cell layers (10): (*i*) the ganglion cell layer; (*ii*) the inner nuclear layer containing bipolar, amacrine, and horizontal cells; and (*iii*) the outer nuclear layer containing photoreceptor cells and their photoreceptor segments. These cell layers are nourished by two separate blood supplies: the retinal and choroidal vasculatures (11), located on either side of the retina. The retinal vasculature, located closest to the vitreous, nourishes the ganglion cell and inner nuclear layers and is embedded primarily within the ganglion cell layer with some capillaries projecting deep into the inner nuclear layer. By contrast, the choroidal vasculature nourishes the avascular outer nuclear layer and is external to the neural retina, sandwiched between the retinal pigment epithelium and the sclera. Importantly, it has been suggested that blood flow in the two vascular beds is regulated differently. Choroidal blood flow exceeds local metabolic requirements and is many times higher than either retinal or cerebral blood flow (12). The retinal and choroidal vessels also respond differently to inhalation stimuli. Retinal vessels strongly vasoconstrict in response to pure oxygen inhalation and vasodilate in response to inhaled carbon dioxide, whereas the choroidal vessels only weakly vasoconstrict in response to pure oxygen and weakly vasodilate in response to carbon dioxide (12, 13).

Many retinal diseases, including retinitis pigmentosa (14), diabetic retinopathy (15), glaucoma, and macular degeneration, progressively affect distinct cellular and vascular layers. Retinitis pigmentosa causes selective loss of the photoreceptor cells with progressive secondary damage to other cellular and vascular layers. Diabetic retinopathy is a multistage disease whose prolonged course typically begins years before diagnosis. Insufficient oxygen delivery and hypoxia associated with the energy-demanding photoreceptors has been implicated in the early stage of the disease.

Author contributions: H.C., M.T.P., P.M.T., D.E.O., and T.Q.D. designed research; H.C., G.N., T.A.W., and M.K.K. performed research; G.N., T.A.W., and M.K.K. contributed new reagents/analytic tools; H.C., G.N., T.A.W., and M.K.K. analyzed data; and M.T.P., P.M.T., and T.Q.D. wrote the paper.

The authors declare no conflict of interest.

This article is a PNAS direct submission.

Abbreviations: Gd-DTPA, gadolinium-diethylene-tri-amine-pentaacetic acid; fMRI, functional MRI; RCS, Royal College of Surgeons; BOLD, blood-oxygen-level-dependent; PVE, partial-volume effect.

[††]To whom correspondence should be addressed at: Yerkes Imaging Center, Emory University, 954 Gatewood Road NE, Atlanta, GA 30329. E-mail: tduong@emory.edu.

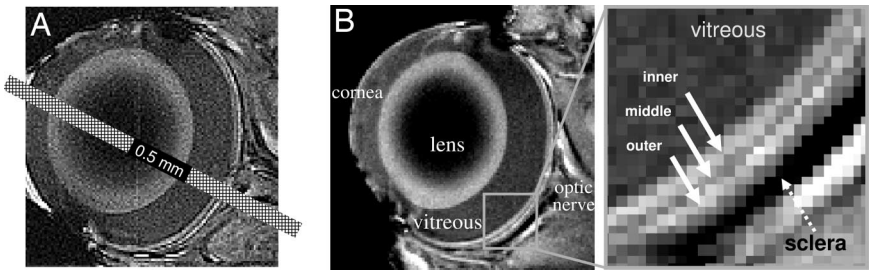


**Fig. 1.** Layer-specific anatomical imaging of the retina. (*A*) A bar depicting a 0.5-mm-thick MRI slice overlaid on an edge-enhancement processed eye image illustrating the potential partial-volume effect. (*B*) Anatomical images at 60 × 60 $\mu$m resolution from a normal adult rat. Three distinct layers (solid arrows) of alternating bright, dark, and bright bands are evident. Sclera (dashed arrow) appears hypointense.

This oxygen delivery-utilization mismatch ultimately precipitates late stage neovascularization and vision loss. Techniques to localize structural, physiological, and functional changes to specific cellular and vascular layers *in vivo* should improve early diagnosis, tracking of disease progression, and monitoring of treatment efficacies.

We report layer-specific structural MRI and BOLD fMRI of rat retina *in vivo*. Structural MRI reveals three distinct bands that correlate histologically with known laminar structures. fMRI reveals layer-specific and differential BOLD responses to hyperoxia and hypercapnia. To corroborate sensitivity and specificity, we evaluate an animal model of retinal degeneration, the Royal College of Surgeons (RCS) rat (16), which has a genetic defect shared by some patients with retinitis pigmentosa (14). Photoreceptors in the RCS retina progressively degenerate over the first 3 months of life because of a defect in the retinal pigmented epithelium that prevents proper phagocytosis of the shed photoreceptor segments (17). Consistent with histology, MRI confirms the loss of the outer nuclear layer and photoreceptor segments. Importantly, MRI reveals altered thickness of the choroidal vascular layer and perturbed vascular reactivity, secondary to photoreceptor cell loss. These results indicate that laminar-specific structural, physiological, and functional MRI of the retina can provide clinically relevant information about retinal physiology and layer-specific changes associated with retinal disease without depth limitation.

## Results

**Lamina-Specific Structural MRI.** Rat eyes were measured to be 6–7 mm in diameter. Assuming a 6-mm diameter sphere, we calculated the partial-volume effect (PVE) due to the curvature of the retina to be 3% and 13% of the total retinal thickness (see below) for midsagittal imaging slices of 0.5 and 1 mm, respectively. Because the posterior retina is relatively flat, these calculations should reflect the upper limits of PVE. Fig. 1*A* depicts a scaled 0.5-mm MRI slice superimposed on an eye image to illustrate the negligible PVE arising from the curved retina.

Fig. 1*B* depicts an image of a normal retina, revealing three distinct "layers" as indicated by the alternating bright, dark, and bright bands. The vitreous and the sclera appeared relatively hypointense because of the long $T_1$ constant of the vitreous water and the low water content and short $T_2^*$ of the sclera (18). Administration of the i.v. contrast agent Gd-DTPA markedly enhanced retinal boundaries (Fig. 2), consistent with the localization of Gd-DTPA impermeable vasculature on either side of the retina. The outer strip was thicker and more enhanced than the inner strip. In contrast, no enhancement was observed in the middle band, lens or vitreous. The Gd-DTPA-enhanced inner and outer strips correlated, respectively, with the inner and outer bands of the images without Gd-DTPA.

Retinal images were virtually flattened and intensity profiles obtained to calculate laminar thicknesses (Fig. 3). To verify the robustness of thickness determination, simulation studies were performed by using parameters shown in Fig. 3 and sampling of 60 $\mu$m per pixel resolution at two noise levels (Gaussian noise 1 and 8 times that of vitreous) (Fig. 4). Accurate results were obtained even with noise eight times the *in vivo* data for the experimental contrast, signal-to-noise ratio, and band separations.

To assign MRI-derived retinal layers, images were compared with standard histology. A histologic section depicting standard cell layers, the embedded retinal vascular layer, and a distinct choroidal vascular layer is shown in Fig. 5. Comparative analysis yielded the following layer assignments. The inner MRI band correlated with the combined ganglion cell layer/inner nuclear layer plus the embedded retinal vessels. Consistent with the inclusion of a vascular component, Gd-DTPA enhanced this band. The middle band, which appeared relatively hypointense on anatomical imaging, was not enhanced by Gd-DTPA and was thus assigned the avascular outer nuclear layer and the photoreceptor segments. Gd-DTPA enhanced the outer band, which was assigned the choroidal vascular layer. The inner, middle, and outer band thicknesses of adult Sprague–Dawley rat retinas were, respectively, 92 ± 9, 77 ± 9, and 37 ± 8 $\mu$m by histology (SD, $n = 9$, total thickness = 205 ± 11 $\mu$m), and 101 ± 17, 79 ± 11, and 86 ± 10 $\mu$m by MRI ($n = 24$; total thickness, 267 ± 31 $\mu$m). MRI-derived thicknesses of the inner and middle bands were similar to histologic measurements, whereas the outer band was significantly thicker than the histology-derived thickness of the choroidal vascular layer. The group-average inner-to-outer peak spacing was 162 ± 26 $\mu$m.

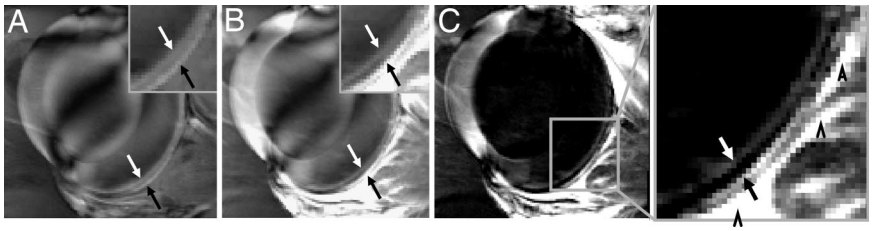


**Fig. 2.** Contrast-enhanced MRI delineating two vascular layers bounding the retina. (*A* and *B*) Contrast-enhanced images at 60 × 60 $\mu$m before (*A*) and after (*B*) Gd-DTPA administration. (*C*) The subtracted image. The two arrows in the expanded views indicate the inner and outer bands of the retina corresponding to the two vascular layers bounding the retina. The dark lines across the lens arose from magnetic and radiofrequency heterogeneity. Three arrowheads indicate signal enhancement of extraocular tissues supplied by Gd-DTPA permeable vessels.

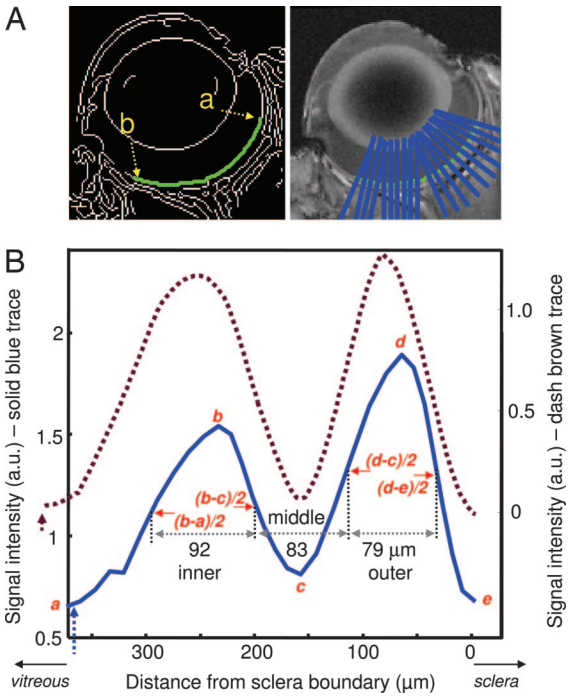


**Fig. 3.** Automated determination of MRI retinal thicknesses. (*A*) The retina was segmented by using an edge-detection technique (green trace). Retinal thickness was quantified from point a to point b, cognizant of the irregular retinal thickness from the posterior pole to the pars plana. (*B*) Intensity profiles of two animals delineate the outer, middle, and inner bands. The vertical dashed arrows indicate the vitreous boundary. Values in micrometers indicate the band thicknesses of the solid trace.

**Lamina-Specific BOLD fMRI.** Dynamic BOLD fMRI was used to probe the lamina-specific responses to hyperoxia and hypercapnia. Robust layer-specific BOLD fMRI responses were detected in the normal retina. Importantly, the two vascular layers responded differently to inhalation stimuli. Hyperoxia induced a larger BOLD response in the outer band (12 ± 2%, $n = 8$) than the inner band (7 ± 2%, $P < 0.01$) (Fig. 6*A*). In contrast, hypercapnia induced a smaller BOLD response in the outer band (1.6 ± 1%, $n = 8$) than in the inner band (10 ± 2%, $P < 0.01$) (Fig. 6*B*). Small BOLD responses detected in the middle band (hyperoxia: 1.5 ± 1% and hypercapnia: 1.2 ± 1.5%) were likely due in large part to PVE from adjacent bands.

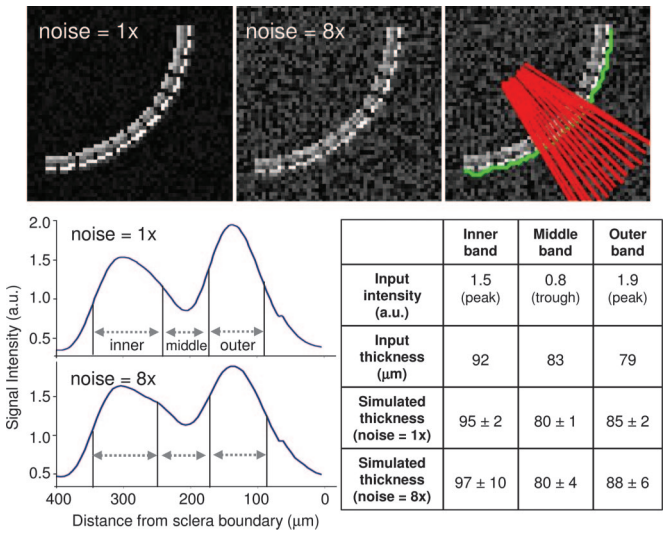


| | Inner band | Middle band | Outer band |
|---|---|---|---|
| Input intensity (a.u.) | 1.5 (peak) | 0.8 (trough) | 1.9 (peak) |
| Input thickness (μm) | 92 | 83 | 79 |
| Simulated thickness (noise = 1x) | 95 ± 2 | 80 ± 1 | 85 ± 2 |
| Simulated thickness (noise = 8x) | 97 ± 10 | 80 ± 4 | 88 ± 6 |

**Fig. 4.** Simulations to validate MRI thickness determination. (*Upper*) Simulated retinas were constructed based on parameters in Fig. 3 and sampled at 60 μm per pixel. (*Lower Left*) Two noise levels were evaluated (Gaussian noise of 1 and 8 times that of vitreous). The retina was segmented (green trace), and an intensity profile was obtained. (*Lower Right*) Comparison of the input and simulated thicknesses showed accurate width determination given the contrast, signal-to-noise ratio, and band separations. Note that the midpoint intensities are not at the same height.

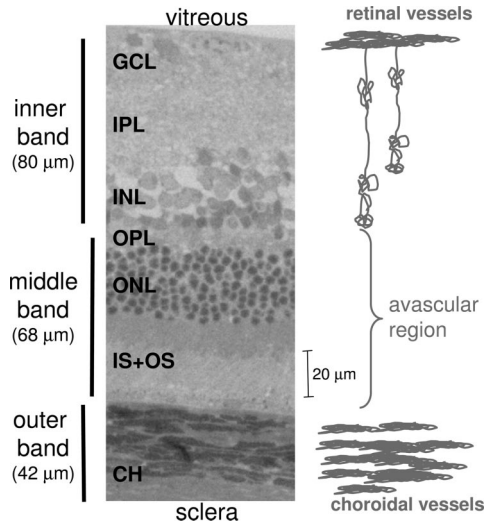


**Fig. 5.** Histological section of a normal adult Sprague–Dawley rat retina stained with toluidine blue. Three vertical bars on the left show the assignments of the three MRI-derived layers. GCL, ganglion cell layer; IPL, inner plexiform layer; INL, inner nuclear layer; OPL, outer plexiform layer; ONL, outer nuclear layer; IS+OS, inner and outer photoreceptor segment; CH, choroidal vascular layer.

**Lamina-Specific MRI Revealed Changes in Photoreceptor Degeneration.** To further corroborate the sensitivity and specificity of layer-specific MRI, we investigated retinas of RCS rats by comparing imaging results obtained at postnatal day 16 (P16, control) and P120. At P16, the photoreceptor layer and the

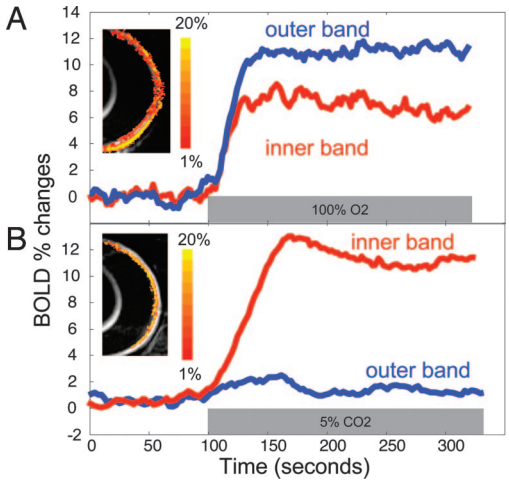


**Fig. 6.** Differential layer-specific BOLD fMRI of the retina. Lamina-specific BOLD fMRI responses to hyperoxia (100% $O_2$) (*A*) and hypercapnia (5% $CO_2$ in air) (*B*) from a normal rat at 90 × 90 μm in-plane resolution. BOLD percent-change maps are overlaid on echoplanar images. The color bar indicates 1–20% BOLD changes.

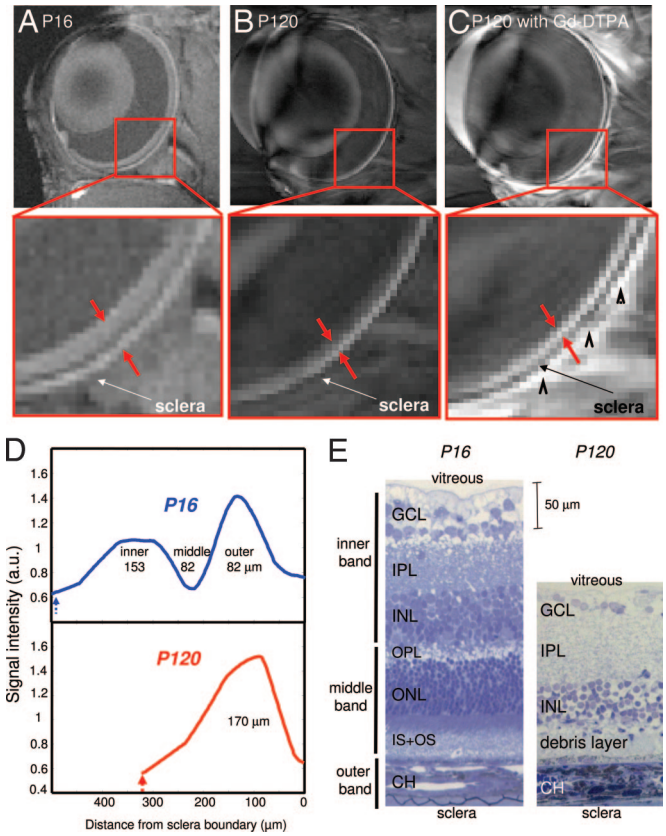


**Fig. 7.** Anatomical MRI and histology of retinal degeneration. (*A–C*) Anatomical images at 60 × 60 $\mu$m resolution of P16 RCS retina before photoreceptor degeneration (control) (*A*), and degenerated P120 RCS retina before (*B*) and after (*C*) i.v. administration of Gd-DTPA. The arrowheads in *C* indicate signal enhancement of extraocular tissues. (*D* and *E*) Intensity profiles (*D*) and histological sections (*E*) show thinning of the P120 compared with the P16 RCS retina. The dashed blue and red arrows in *D* indicate the vitreous boundaries.

photoreceptor segments of RCS rats are histologically intact, whereas, by P120, they have completely degenerated. Three distinct layers were visible at P16 (Fig. 7*A*). However, only a single band was visible at P120 (Fig. 7*B*). We found that i.v. Gd-DTPA administration enhanced the entire retinal thickness in the P120 RCS rat (Fig. 7*C*), consistent with the loss of the avascular outer nuclear layer and the photoreceptor segments. Intensity profiles revealed an absent middle band and an overall thinning of the P120 RCS retina (Fig. 7*D*). Interestingly, the outer band appeared slightly thickened.

The loss of the photoreceptor layer in P120 RCS retinas was confirmed by histological analysis (Fig. 7*E*). In place of the photoreceptors and photoreceptor segments, only a thin debris layer was visible in the P120 RCS retina, and the total thickness was markedly reduced. Laminar thicknesses of the P16 and P120 RCS retinas are summarized in Table 1. As an aside, the retinal thickness of the P16 RCS rat was thicker than that of normal adult Sprague–Dawley rats, likely because of strain and/or age differences which require further investigation.

BOLD fMRI associated with hyperoxia and hypercapnia was also performed on P120 RCS rats. In the P120 RCS retinas, BOLD fMRI responses to hyperoxia in both vascular layers were attenuated (inner band: 4.2 ± 2.5% and outer band: 8.7 ± 2.4%, $n = 4$) and the BOLD fMRI responses to hypercapnia largely disappeared (inner band: −0.02 ± 6.5% and outer band: 0.003 ± 6%), demonstrating perturbation of vascular reactivity secondary to photoreceptor loss.

**Table 1. Layer thicknesses (in micrometers) of P16 and P120 RCS rat retinas (Long–Evans rats)**

| | RCS P16 | | RCS P120 | |
|---|---|---|---|---|
| Bands | MRI ($n = 6$) | Histology ($n = 5$) | MRI ($n = 4$) | Histology ($n = 4$) |
| Inner | 157 ± 6 | 167 ± 31* | — | 101 ± 21* |
| Middle | 99 ± 17 | 112 ± 20 | — | 29 ± 8 |
| Outer | 95 ± 15* | 34 ± 4* | — | 35 ± 1 |
| Total | 350 ± 13 | 307 ± 41 | 169 ± 13 | 169 ± 23 |

Data are given as means ± SD. *, $P < 0.05$.

## Discussion

Structural MRI reveals three discernable layers in normal retina as validated by histology. Gd-DTPA enhanced MRI delineates two vascular layers bounding the retina, confirming the avascularity of the outer nuclear layer. BOLD fMRI shows lamina-specific and differential responses to physiologic challenges. Moreover, in an accepted animal model of photoreceptor degeneration, layer-specific MRI correctly identifies the disappearance of the outer nuclear layer and photoreceptor segments, further corroborating layer assignments. Finally, MRI reveals a newly identified thickening of the choroidal vascular layer and perturbed vascular reactivity in RCS retinas.

**Laminar Structures.** Our assignment of MRI bands is supported by both general histologic assessment and correlations between histologic and MRI-derived laminar thicknesses. MRI-derived thicknesses of the neural retina, as reflected by the inner and middle bands, agree with histological measurements performed by us and others (19, 20). In contrast, the outer band as measured by MRI was significantly thicker than the histological determination of the choroidal vascular layer. We found only a single report of choroidal thickness (25–45 $\mu$m) determined by histology (21). The discrepancy between the *in vivo* and histologic data could arise from collapse of choroidal vessels after removal of orbits from the systemic circulation, histological shrinkage, and/or PVE because of limited MRI spatial resolution, underscoring the importance of measurements *in vivo*.

Subtraction of post- and pre-Gd-DTPA contrast images showed marked signal enhancement on either side of the retina. Greater Gd-DTPA enhancement of the outer band compared with the inner band is consistent with the higher blood flow and volume in the choroidal compared with the retinal vasculature (12). High choroidal blood flow appears necessary to maintain a large oxygen gradient to facilitate oxygen delivery to the avascular outer nuclear layer (22) and/or dissipate heat produced by incident light (23). In fact, the oxygen tension in the inner nuclear layer and outer nuclear layer is close to zero under normal physiologic conditions (24, 25). These MRI results are in agreement with our recent report in which three major cell layers were also observed in cat retinas, albeit at lower spatial resolution (18). Taken together, the MRI layer assignments are consistent with known layer structures of the retina.

**Vascular Couplings and BOLD Responses.** Coupling of blood flow, oxygenation, and metabolism in the brain has been well described. However, experimental evidence of such coupling in the retina was reported only recently. Flickering light increases retinal and optic nerve head blood flow, as determined by a Laser Doppler flow measurement (26). Physiologic respiratory challenges with oxygen or carbogen modulate tissue oxygenation, as measured by oxygen polarographic electrodes (27). Visual stimulation modulates optical absorption and/or scattering as detected by intrinsic optical imaging (3, 34). Finally, visual-evoked BOLD fMRI of the retina (28) has been reported.

None of these studies, however, provides lamina-specific resolution.

Our BOLD fMRI data, demonstrating the layer-specific and differential responses to hyperoxia and hypercapnia in the two vascular layers, are consistent with Laser Doppler flow (2) and oxygen-electrode (27) measurements, despite the fact that all three techniques measure different (but related) aspects of retinal physiology and have different signal sources. Inhalation of pure oxygen increases capillary and venous oxygen saturation and thus increases the BOLD signal (4). Note that the arteriovenous oxygen difference in the choroid is small compared with the brain (12), and, thus, one might expect a small hyperoxia-induced BOLD increase. However, strong hyperoxia-induced BOLD increase was detected, likely because the choroid has a high vascular density and/or anesthesia herein could increase arteriovenous oxygen difference, amplifying the hyperoxia-induced BOLD increase. More importantly, hyperoxia-induced BOLD signal showed a larger increase in the outer band (choroidal vascular layer) than in the inner band (retinal vascular layer). This is likely because hyperoxia is known to markedly decrease retinal blood flow by 60% (29, 30), which counteracts the BOLD signal increase from elevated oxygen tension by hyperoxia *per se*. In contrast, hyperoxia does not significantly affect choroidal blood flow (29, 30). The higher choroidal vascular density in the outer band compared with the retinal vascular density in the inner band could further amplify the differential BOLD responses between the two vasculatures.

Carbon dioxide inhalation causes vasodilation and increased blood flow in the brain, which leads to a decreased fractional oxygen extraction and increased capillary and venous oxygen saturation (4). Thus, hypercapnia is expected to increase BOLD signal. In the retina, hypercapnia strongly vasodilates retinal vessels, whereas it has a much smaller vasodilatory effect on choroidal blood vessels (12, 29). Consistent with the vasodilatory response, the BOLD signal increase in the inner band containing the retinal vessels was larger than in the outer band. Together, these results support the contention that the two vascular supplies to the retina are differentially regulated.

**Lamina-Specific Changes in Retinal Degeneration.** Photoreceptor degeneration in RCS rats has been well characterized, providing an excellent model to evaluate specificity and sensitivity of layer-specific MRI. The RCS retina photoreceptor layer is normal at P16 but degenerates progressively and disappears completely by P90 (16, 27). MRI has sufficient sensitivity and specificity to detect the loss of the photoreceptor layer in P120 animals. Moreover, MRI revealed an apparent thickening of the choroidal layer. This thickening could be because of actual choroid thickening and/or inclusion of the residual degenerated photoreceptor layer. Not unexpectedly, the debris layer appeared to develop edema, which resulted in increased signal intensity. Gd-DTPA experiments, although confounded by PVE, suggested this debris layer was permeable to Gd-DTPA. Breakdown of the blood-retinal barrier to horseradish peroxidase, invasion of retinal-pigmented-epithelium cells into the outer nuclear layer, and neovascularization in RCS retina have been reported (31).

With the observed structural changes, it is reasonable to postulate that neural-vascular coupling could be perturbed. Hypercapnic and hyperoxic challenges are commonly used to study the vascular reactivity in normal and diseased brains. Attenuated BOLD responses to hyperoxia and hypercapnia were observed in P120 RCS retinas. Diminished BOLD response in the choroidal vasculature is perhaps not surprising because the choroid supplies predominantly the outer nuclear layer. The reduced BOLD response in the retinal vascular layer could be a secondary effect of photoreceptor degeneration (i.e., thinning of the inner band). Our results are consistent with abnormal retinal oxygen profiles in RCS retinas under basal conditions (27). We found no publication describing Laser Doppler flow and intrinsic optical imaging of the RCS retinas. These findings, if confirmed, could have important implications.

In summary, we report noninvasive, high-resolution MRI detection of lamina-specific structures and functional responses in the *in vivo* retina. These technologies have the potential to provide powerful insights into how retinal and choroidal oxygenation are regulated and how retinal diseases may affect the two vasculatures and the neural tissues they subserve. Further improvement in spatial resolution is expected. Given the remarkable progresses in MRI technologies made on imaging the brain, translating these technologies to longitudinally study the retina could critically impact retinal research.

## Materials and Methods

**Animal Preparation.** Three groups of rats were studied: (*i*) normal adult Sprague–Dawley rats ($n = 24$, 275–350 g), (*ii*) Long–Evans RCS rats of postnatal day 16 (P16) ($n = 6$, range: P16–20) before photoreceptor degeneration, and (*iii*) Long–Evans RCS rats of P120 ($n = 4$, range: P120-P270, 275–350g) after photoreceptor degeneration. In group 1, MRI thicknesses were obtained on all 24 rats, histology on a subset of nine rats, and fMRI on eight rats. In group 2, structural MRI and histology were performed on all six rats with histology from one rat unsuccessful. In group 3, structural, functional MRI and histology studies were performed on all four rats.

A femoral vein was catheterized for remote i.v. Gd-DTPA administration (0.4 ml/kg, 0.5 M) during imaging. Animals were anesthetized with ≈1% isoflurane, paralyzed with pancuronium bromide (3 mg/kg first dose, 1 mg/kg/hr, i.p.), and mechanically ventilated. End-tidal $CO_2$ (Surgivet capnometer), heart rate, and arterial $O_2$ saturation (Nonin-8600) and rectal temperature were continuously monitored and maintained within normal physiologic ranges unless purposefully altered. Blood gases were sampled in some animals, and all sampled blood gases were within normal physiologic or targeted ranges.

**Inhalation Stimuli.** Hyperoxic (100% $O_2$) and hypercapnic (5% $CO_2$, 21% $O_2$, balance $N_2$) challenges were used to modulate tissue oxygenation and blood flow. Ambient air was used as a baseline. Images were acquired continuously in 320-s blocks (100 s during baseline and 220 s hyperoxia or hypercapnia) with at least 10-min intervals between blocks.

**MRI.** MRI studies were performed on a Bruker 4.7-Tesla/40-cm magnet (Billerica, MA). Rats were placed onto a head holder consisting of ear and tooth bars. MRI was performed on a single midsagittal slice at the center of the left eye by using a small surface coil (inner diameter ≈1 cm). Anatomical MRI was obtained by using a gradient-echo pulse sequence with a repetition time of 150 ms, echo time of 3.5 ms, three 0.5-mm slice thickness, 32 repetitions, 128 × 128 data matrix, and 7.7 × 7.7 mm field of view, yielding a 60 × 60 $\mu$m in-plane resolution in 10 min.

BOLD fMRI was obtained by using two-segment, spin-echo, diffusion-weighted, echo-planar imaging. Diffusion-weighted preparation was used to suppress the otherwise overwhelmingly strong, fast-diffusing water signal from the vitreous (18). The fMRI parameters were: repetition time = 1 s per segment, echo time = 51 ms, 1.0-mm slice thickness, time between applications of two diffusion gradient pulses ($\Delta$) = 20 ms, diffusion gradient pulse duration ($\delta$) = 3.5 ms, $b$ value = 450 s/mm$^2$, 128 × 128 data matrix, and 11.5 × 11.5 mm field of view, yielding a 90 × 90 $\mu$m in-plane resolution. Each fMRI block took 320 s.

Four to six repeated measurements were typically made for anatomical and for functional MRI of each gas conditions on each animal. Gd-DTPA MRI was performed once on each rat.

**Image Data Analysis.** Data analysis was performed by using Matlab and Stimulate software (University of Minnesota, Minneapolis, MN). All images were acquired in time series and corrected for motion and drift before averaging pixel-by-pixel offline as needed. To quantitatively determine the laminar thickness, the retina was automatically detected by using an edge-detection technique. Radial projections perpendicular to the vitreous boundary were obtained with nine times the sampling density of the original image (equivalent to spatial interpolation). The projection profiles were averaged into intensity profiles (Fig. 3). Band thicknesses were determined by using the "half height" method (32, 33), widely used to measure vessel diameters in optical imaging studies. The midpoint between the minimum and maximum intensities at each boundary was first determined (the trough between the two peaks was considered as one of the minima). The band thickness was then determined as the horizontal distance between two neighboring mid-intensity points which were not necessarily at the same heights (32, 33) (see Fig. 3). This analysis was performed automatically by using Matlab. In addition, simulations were performed to evaluate the robustness of this approach (Fig. 4). Curved retinas were simulated based on parameters in Fig. 3 (solid trace) and sampled with 60 $\mu$m per pixel resolution. Ten simulations were performed with two noise levels (Gaussian noise of 1 and 8 times that of vitreous). Identical processing was applied to obtain band thicknesses. Given our experimental contrast-to-noise ratio, signal-to-noise ratio, and band separations, this approach yielded robust thicknesses consistent with histology. An alternative approach based on objective modeling of two Gaussians was also used to support the band thickness determination. These results, shown in Fig. 8, which is published as supporting information on the PNAS web site, are consistent with those by using the half height method.

Cross correlation analysis with 90% confident level was performed by matching the fMRI signal time courses to the stimulus paradigm to calculate the BOLD percent-change maps which were overlaid on echo-planar images. A minimal cluster size of 4–8 contiguous pixels was further imposed with a resultant $P \ll 0.01$. Three equal bands on normal rat retinas or two equal bands on P120 RCS retinas after photoreceptor degeneration were automatically identified. BOLD percent changes in these bands were tabulated without bias toward "active" pixels, providing objective measures for comparison between normal and P120 RCS rats. Data are presented as mean $\pm$ SD. Student $t$ test was used with $P < 0.05$ indicating statistical significance.

**Histology.** Standard histology was performed on tissue sections corresponding to MRI slices. Eyes were enucleated and immersion fixed overnight in 2% paraformaldehyde. Eyes were rinsed in 0.1 M phosphate buffer, dissected to isolate the posterior eyecup, embedded in epoxy-resin, sectioned at 0.5 $\mu$m, and stained with toluidine blue. Each histological section was digitally photographed. Thickness of different layers of the neural retina and choroidal vasculature were semiautomatically derived by using an image analysis program (Image Pro, Cybernetics, Silver Spring, MD).

This work was supported by Whitaker Foundation Grant RG02-0005, National Eye Institute Grant R01EY014211, the Department of Veterans Affairs, and National Center for Research Resources Grant P51RR00165.

1. Fujimoto JG, Pitris C, Boppart SA, Brezinski ME (2000) *Neoplasia* 2:9–25.
2. Riva CE, Cranstoun SD, Mann RM, Barnes GE (1994) *Invest Ophthalmol Vis Sci* 35:608–618.
3. Grinvald A, Bonhoeffer T, Vanzetta I, Pollack A, Aloni E, Ofri R, Nelson D (2004) *Ophthalmol Clin North Am* 17:53–67.
4. Ogawa S, Lee T-M, Kay AR, Tank DW (1990) *Proc Natl Acad Sci USA* 87:9868–9872.
5. Kim D-S, Duong TQ, Kim S-G (2000) *Nat Neurosci* 3:164–169.
6. Duong TQ, Kim D-S, Ugurbil K, Kim S-G (2001) *Proc Natl Acad Sci USA* 98:10904–10909.
7. Cheng K, Waggoner RA, Tanaka K (2001) *Neuron* 32:359–397.
8. Silva AC, Koretsky AP (2002) *Proc Natl Acad Sci USA* 99:15182–15187.
9. Goense JB, Logothetis NK (2006) *Magn Reson Imag* 24:381–392.
10. Wassle H, Boycott BB (1991) *Physiol Rev* 1:447–480.
11. Harris A, Kagemann L, Cioffi GA (1998) *Surv Ophthalmol* 42:509–533.
12. Bill A (1984) in *Handbook of Physiology Part 2 in Microcirculation*, eds Renkin EM, Michel CC (Am Physiol Soc, Bethesda, MD), pp 1001–1035.
13. Sharma RJ, Ehinger BEJ (1992) in *Alder's Physiology of the Eye*, eds Kaufman PL, Alm A (Mosby, St. Louis, MO), pp 319–348.
14. Gal A, Li Y, Thompson DA, Weir J, Orth U, Jacobson SG, Apfelstedt-Sylla E, Vollrath D (2000) *Nat Genet* 26:270–271.
15. Frank RN (2004) *N Engl J Med* 350:48–58.
16. Dowling JE, Sidman RL (1962) *J Cell Bio* 14:73–109.
17. D'Cruz PM, Yasumura D, Weir J, Matthes MT, Abderrahim H, LaVail MM, Vollrath D (2000) *Hum Mol Genet* 9:645–651.
18. Shen Q, Cheng H, Chang TF, Nair G, Shonat RD, Pardue MT, Toi VV, Duong TQ (2006) *J Magn Reson Imaging* 23:465–472.
19. Buttery RG, Hinrichsen CFL, Weller WL, Haight JR (1991) *Vision Res* 31:169–187.
20. Thomas BB, Arai S, Ikai Y, Qiu G, Chen Z, Aramant RB, Sadda SR, Seiler MJ (2006) *J Neurosci Methods* 151:186–193.
21. Steinle JJ, Smith PG (2002) *Br J Pharmacol* 136:730–734.
22. Linsenmeier RA, Padnick-Silver L (2000) *Invest Ophthalmol Vis Sci* 41:3117–3123.
23. Parver LM (1980) *Am J Ophthalmol* 89:641–646.
24. Linsenmeier RA (1986) *J Gen Physiol* 88:521–542.
25. Yu D-I, Cringle SJ, Alder V, Su E-N (1999) *Invest Ophthalmol Vis Sci* 40:2082–2087.
26. Riva CE, Harino S, Shonat RD, Petrig BL (1991) *Neurosci Lett* 128:291–296.
27. Yu D-Y, Cringle SJ, Su E-N, Yu PK (2000) *Invest Ophthalmo Vis Sci* 41:3999–4006.
28. Duong TQ, Ngan S-C, Ugurbil K, Kim S-G (2002) *Invest Ophthalmol Vis Sci* 43:1176–1181.
29. Trokel S (1965) *Arch Ophthalmol* 73:838–842.
30. Riva CE, Grunwald JE, Singclair SH (1983) *Invest Ophthalmol Vis Sci* 24:47–51.
31. Wang S, Villegas-Perez MP, Holmes T, Lawrence MM, Vidal-Sanz M, Hurtado-Montalban N, Lund RD (2003) *Current Eye Res* 27:183–196.
32. Eaton AM, Hatchell DL (1988) *Invest Ophthalmo Vis Sci* 29:1258–1264.
33. Newsom RS, Sullivan PM, Rassam SM, Jagoe R, Kohner EM (1992) *Graefes Arch Clin Exp Ophthalmol* 230:221–225.
34. Tsunoda K, Oguchi Y, Hanazona G, Tanifuji M (2004) *Invest Ophthalmol Vis Sci* 45:3820–3826.